The Journal of Chemical Physics

Revisiting impulsive stimulated thermal scattering in supercooled liquids: Relaxation of specific heat and thermal expansion

Cite as: J. Chem. Phys. **155**, 164501 (2021); https://doi.org/10.1063/5.0063805
Submitted: 17 July 2021 • Accepted: 06 October 2021 • Accepted Manuscript Online: 06 October 2021 • Published Online: 22 October 2021

Marco Gandolfi, Liwang Liu, Pengfei Zhang, et al.

AIP Publishing

The Journal of Chemical Physics ARTICLE scitation.org/journal/jcp

Revisiting impulsive stimulated thermal scattering in supercooled liquids: Relaxation of specific heat and thermal expansion

Cite as: J. Chem. Phys. 155, 164501 (2021); doi: 10.1063/5.0063805
Submitted: 17 July 2021 • Accepted: 6 October 2021 •
Published Online: 22 October 2021

Marco Gandolfi,[1,2,3,4,5,a)] Liwang Liu,[3,a)] Pengfei Zhang,[3] Mansour Kouyaté,[3] Robbe Salenbien,[6,7] Francesco Banfi,[8] and Christ Glorieux[3]

AFFILIATIONS

[1] CNR-INO (National Institute of Optics), Via Branze 45, 25123 Brescia, Italy
[2] Department of Information Engineering, University of Brescia, Via Branze 38, 25123 Brescia, Italy
[3] Laboratory of Soft Matter and Biophysics, Department of Physics and Astronomy, KU Leuven, Celestijnenlaan 200D, B-3001 Leuven, Belgium
[4] Dipartimento di Matematica e Fisica, Università Cattolica del Sacro Cuore, Via Musei 41, 25121 Brescia, Italy
[5] Interdisciplinary Laboratories for Advanced Materials Physics (I-LAMP), Via Musei 41, 25121 Brescia, Italy
[6] VITO, Boeretang 200, Mol 2400, Belgium
[7] EnergyVille, Energyville I, Thor Park 3800, Genk 3600, Belgium
[8] FemtoNanoOptics Group, Université de Lyon, CNRS, Université Claude Bernard Lyon 1, Institut Lumière Matière, F-69622 Villeurbanne, France

[a)] **Authors to whom correspondence should be addressed:** marco.gandolfi@ino.cnr.it and liwang.liu@kuleuven.be

ABSTRACT

Impulsive stimulated thermal scattering (ISTS) allows one to access the structural relaxation dynamics in supercooled molecular liquids on a time scale ranging from nanoseconds to milliseconds. Till now, a heuristic semi-empirical model has been commonly adopted to account for the ISTS signals. This model implicitly assumes that the relaxation of specific heat, C, and thermal expansion coefficient, γ, occur on the same time scale and accounts for them via a single stretched exponential. This work proposes two models that assume disentangled relaxations, respectively, based on the Debye and Havriliak–Negami assumptions for the relaxation spectrum and explicitly accounting for the relaxation of C and γ separately in the ISTS response. A theoretical analysis was conducted to test and compare the disentangled relaxation models against the stretched exponential. The former models were applied to rationalize the experimental ISTS signals acquired on supercooled glycerol. This allows us to simultaneously retrieve the frequency-dependent specific heat and thermal expansion up to the sub-100 MHz frequency range and further to compare the fragility and time scale probed by thermal, mechanical, and dielectric susceptibilities.

I. INTRODUCTION

The intriguing behavior of glass-forming liquids is the object of a continuous research effort.[1–9] By virtue of its ability to simultaneously probe multiple relaxation processes, such as thermal expansion, acoustic, and orientational response,[10,11] the use of impulsive stimulated thermal scattering (ISTS) in a periodical grating geometry allowed gaining new insights from the thermoelastic response to impulsive photothermal excitation in several glass formers.[11–17] Standard thermo-mechanical modeling,[18] based on the assumption of frequency-independent (non-relaxing) specific heat and thermal expansion coefficient, has been shown to be inadequate to characterize the dynamics triggered in an ISTS experiment, this being especially true for viscous systems. Along with the first experimental ISTS results, a semi-empirical "entangled" (SE) model,[18] relying on a stretched exponential function to describe the initial thermal

expansion rise of the ISTS signal, proved effective in describing the ISTS response of glycerol, salol, and DC704 oil.[12,14,18] The latter model accounts for the concomitant volume and temperature change upon system's heating. The intertwining of these two effects may be traced to an increased vibrational amplitude and increased average interatomic distance (volume increase) with a concomitant population of higher energy levels (temperature increase).

Inspired by successful descriptions of the temperature dynamics upon external heating,[19–22] we propose an analytical generalized "disentangled" (DE) model. The model accounts for the relaxation of both C and γ,[6] which are not explicitly considered in the SE model, and enables disentangling their effects on the ISTS signal. The idea is as follows: We first address the thermal diffusion and thermoelastic equations in the frequency domain. In our analytical treatment, we exploit a frequency-dependent specific heat and thermal expansion coefficient following the Debye and Havriliak–Negami (HN) empirical relaxation models, respectively. The calculated temperature response is then inserted as a driving term in the thermoelastic equation, which describes the evolution of the strain field. The strain field variations affect the refractive index and are ultimately encoded in the ISTS signal dynamics. A comparison between the DE and SE models is made by conducting a case study on ISTS data for glycerol reported in the literature.[14,23] Furthermore, a set of newly acquired ISTS signals on supercooled glycerol is analyzed in the frame of the DE model. The procedure allows retrieving $C(\omega)$ and $\gamma(\omega)$ all the way to the sub-100 MHz range. This largely extends the upper limit of the previously accessible bandwidth, 100 kHz[20] and 1 Hz[22,24] for C and γ, respectively, enabling a comparison of relaxation times and fragility values from the obtained heat capacity and thermal expansion with those of mechanical, and dielectric susceptibilities in an extended frequency and temperature range. The relaxation times are cross-checked with a recently reported phenomenological trend ["time scale ordering" or (TSO)].[25]

This paper is organized as follows: Sec. II reports the analytical expressions for the temperature response to impulsive photothermal excitation in a grating geometry. Two scenarios are considered: one for a frequency-independent and the other for a frequency-dependent specific heat and thermal expansion according to the Debye and HN models. In Sec. III, a continuum mechanics thermoelastic model is used to calculate the response of the material strain to photothermal excitation. This is achieved by considering the temperature change as a source term in the equation of motion. A comparison between the results obtained via the proposed DE model approach and simulations performed exploiting the SE model for literature values on glycerol[14] is presented in Sec. IV. Finally, in Sec. V, we apply the developed models to the case of the experimental ISTS signals that we acquired on supercooled glycerol. We compare in detail the thermal, mechanical, and dielectric relaxation for glycerol.

II. TEMPERATURE RESPONSE TO IMPULSIVE PHOTOTHERMAL EXCITATION IN A PERIODIC GRATING GEOMETRY

A. Scenario with frequency-independent specific heat

In this section, we calculate the temperature evolution of a system that is subject to impulsive photothermal excitation generating a transient thermal grating (TTG). For the time being, we assume a frequency-independent specific heat. The starting point is the thermal diffusion equation for the temperature T in a 1D infinite geometry,[26–31]

$$\frac{\partial^2 T}{\partial x^2} - \frac{\rho C}{\kappa_T}\frac{\partial T}{\partial t} = -\frac{Q(x,t)}{\kappa_T}, \tag{1}$$

where ρ (kg m^{-3}), κ_T (W m^{-1} K^{-1}), and C (J kg^{-1} K^{-1}) are the mass density, the thermal conductivity, and the frequency-independent specific heat per unit mass, while $Q(x,t)$ (W m^{-3}) is the heat source. In ISTS experiments, the heat input is impulsive in time and periodical in space,

$$Q(x,t) = \frac{Q_0}{2}[1+\cos(qx)]\delta(t), \tag{2}$$

where Q_0 (J m^{-3}) is the supplied heat density (a positive number) and q (m^{-1}) is the wavenumber, defined as 2π times the inverse of spatial period of the periodical light intensity pattern. The spatial profile of the heat source is periodic, varying from Q_0 in the points of maximum intensity to 0 in the minima. Prior to excitation, the system is at equilibrium at constant temperature T_0.

Upon performing Fourier transform, the following frequency domain expression is obtained:

$$\frac{\partial^2 \tilde{T}}{\partial x^2} - i\omega\frac{\rho C}{\kappa_T}\tilde{T} = -\frac{1}{\kappa_T}\tilde{Q}(x,\omega), \tag{3}$$

and the solution for temperature field (accounting for the initial condition) reads

$$\tilde{T}(x,\omega) = \left(T_0 + \frac{Q_0}{4\rho C}\right)\delta(\omega) + \frac{Q_0}{2i\rho C\omega} + \frac{Q_0}{2i\rho C(\omega - i\alpha q^2)}\cos(qx), \tag{4}$$

where $\alpha = \kappa_T/(\rho C)$ (m^2 s^{-1}) is the thermal diffusivity. By taking inverse Fourier transform, the following expression is obtained for the temperature evolution in space and time coordinates:

$$T(x,t) = T_0 + \frac{Q_0}{2\rho C}\left[1+\cos(qx)\exp\left(-\alpha q^2 t\right)\right]\theta(t), \tag{5}$$

where $\theta(t)$ is the Heaviside step function.

B. Scenario with frequency-dependent specific heat

1. Debye model

The expression for the frequency-dependent specific heat per unit mass in the frame of the Debye model[32] reads

$$C(\omega) = C_\infty + \frac{\Delta C}{1+i\omega\tau_C} = C_\infty + \frac{\Delta C}{1+i\frac{\omega}{\omega_C}}, \tag{6}$$

with C_∞ being the specific heat per unit mass component related to the high-frequency response. In the time domain, this component affects the fast temperature increase following impulsive heating. ΔC is the portion of the specific heat per unit mass that determines the

reduction in the temperature response at low frequencies (that is at frequencies below the relaxation frequency $\omega_C = \tau_C^{-1}$) or, in the time domain, at times longer than the relaxation time τ_C.

Upon substitution of the expression for $C(\omega)$ into Eq. (3), we retrieve the following differential equation:

$$\frac{\partial^2 \tilde{T}}{\partial x^2} - i\omega \frac{\rho}{\kappa_T}\left(C_\infty + \frac{\Delta C}{1 + i\frac{\omega}{\omega_C}}\right)\tilde{T} = -\frac{1}{\kappa_T}\tilde{Q}(x,\omega). \tag{7}$$

Inserting the expression for the heat source $\tilde{Q}(x,\omega)$ obtained transforming in the frequency domain [Eq. (2)], we obtain the following solution:

$$\tilde{T}(x,\omega) = \left[T_0 + \frac{Q_0}{4\rho(C_\infty + \Delta C)}\right]\delta(\omega) - \frac{iQ_0(\omega - i\omega_C)}{2\rho C_\infty\left[\omega - i\omega_C\left(1 + \frac{\Delta C}{C_\infty}\right)\right]\omega} - \frac{iQ_0(\omega - i\omega_C)}{2\rho C_\infty(\omega - \omega_1)(\omega - \omega_2)}\cos(qx), \tag{8}$$

with $\alpha_\infty = \kappa_T/(\rho C_\infty)$ being the high-frequency limit of the thermal diffusivity and

$$\omega_1 = \frac{i}{2}\left\{\left[\alpha_\infty q^2 + \omega_C\left(1 + \frac{\Delta C}{C_\infty}\right)\right] - \sqrt{\left[\alpha_\infty q^2 + \omega_C\left(1 + \frac{\Delta C}{C_\infty}\right)\right]^2 - 4\alpha_\infty q^2 \omega_C}\right\}, \tag{9}$$

$$\omega_2 = \frac{i}{2}\left\{\left[\alpha_\infty q^2 + \omega_C\left(1 + \frac{\Delta C}{C_\infty}\right)\right] + \sqrt{\left[\alpha_\infty q^2 + \omega_C\left(1 + \frac{\Delta C}{C_\infty}\right)\right]^2 - 4\alpha_\infty q^2 \omega_C}\right\}. \tag{10}$$

The angular frequencies ω_1 and ω_2 carry information on the heat capacity relaxation, which is also visible in the thermal diffusion tail of the signal.

The impulse temperature increase, triggered by an impulsive heating source, is obtained by inverse Fourier transform of Eq. (8) (see Sec. I of the supplementary material for more details). We thus obtain

$$\begin{aligned} T(x,t) &= T_0 + \frac{Q_0}{2\rho(C_\infty + \Delta C)}\left\{1 + \frac{\Delta C}{C_\infty}\exp\left[-\omega_C\left(1 + \frac{\Delta C}{C_\infty}\right)t\right]\right\}\theta(t) + \frac{Q_0}{2\rho C_\infty}\cos(qx) \times \left[\frac{(\omega_1 - i\omega_C)}{(\omega_1 - \omega_2)}\exp(i\omega_1 t) + \frac{(\omega_2 - i\omega_C)}{(\omega_2 - \omega_1)}\exp(i\omega_2 t)\right]\theta(t) \\ &= T_0 + \frac{Q_0}{2\rho(C_\infty + \Delta C)}\left\{1 + \frac{\Delta C}{C_\infty}\exp\left[-\omega_C\left(1 + \frac{\Delta C}{C_\infty}\right)t\right]\right\}\theta(t) \\ &\quad + \frac{Q_0}{2\rho C_\infty}\cos(qx)\exp\left\{-\frac{t}{2}\left[\alpha_\infty q^2 + \omega_C\left(1 + \frac{\Delta C}{C_\infty}\right)\right]\right\}\left\{\cosh\left(\frac{t}{2}\sqrt{\left[\alpha_\infty q^2 + \omega_C\left(1 + \frac{\Delta C}{C_\infty}\right)\right]^2 - 4\alpha_\infty q^2\omega_C}\right)\right. \\ &\quad \left. - \frac{\left[\alpha_\infty q^2 + \omega_C\left(\frac{\Delta C}{C_\infty} - 1\right)\right]}{\sqrt{\left[\alpha_\infty q^2 + \omega_C\left(1 + \frac{\Delta C}{C_\infty}\right)\right]^2 - 4\alpha_\infty q^2\omega_C}}\sinh\left(\frac{t}{2}\sqrt{\left[\alpha_\infty q^2 + \omega_C\left(1 + \frac{\Delta C}{C_\infty}\right)\right]^2 - 4\alpha_\infty q^2\omega_C}\right)\right\}\theta(t). \end{aligned} \tag{11}$$

2. Havriliak–Negami model

The Debye model does not fully account for the dynamic of many glass-forming materials. For this reason, the generalized Havriliak–Negami (HN) model[33] was introduced. The HN model introduces two additional model parameters a_C and b_C, reading

$$C(\omega) = C_\infty + \frac{\Delta C}{\left[1 + (i\omega\tau_C)^{a_C}\right]^{b_C}} = C_\infty + \frac{\Delta C}{\left[1 + \left(i\frac{\omega}{\omega_C}\right)^{a_C}\right]^{b_C}}. \tag{12}$$

The HN model converges to the Debye model when $a_C = b_C = 1$. Within the HN model, the temperature response in the frequency domain reads

$$\tilde{T}(x,\omega) = \left[T_0 + \frac{Q_0}{4\rho(C_\infty + \Delta C)}\right]\delta(\omega) - \frac{iQ_0\left[\omega_C^{a_C} + (i\omega)^{a_C}\right]^{b_C}}{2\rho\omega C_\infty\left\{\left[\omega_C^{a_C} + (i\omega)^{a_C}\right]^{b_C} + \frac{\Delta C}{C_\infty}\omega_C^{a_C b_C}\right\}} - \frac{iQ_0\left[\omega_C^{a_C} + (i\omega)^{a_C}\right]^{b_C}\cos(qx)}{2\rho C_\infty\left\{\omega\left[\omega_C^{a_C} + (i\omega)^{a_C}\right]^{b_C} + \frac{\Delta C}{C_\infty}\omega\omega_C^{a_C b_C} - i\alpha_\infty q^2\left[\omega_C^{a_C} + (i\omega)^{a_C}\right]^{b_C}\right\}}. \tag{13}$$

Exponents a_C and b_C are typically non-integer, making inverse Fourier transform of the latter expression rather involved. For this reason, inverse Fourier transform was performed numerically, at variance with the Debye model case.

III. ISTS SIGNAL

A. Constitutive equation

Impulsive stimulated thermal scattering results from the optical diffraction of a probe beam impinging on a spatially periodic strain grating optically patterned in a sample. The ISTS signal is proportional to the strain magnitude. In this subsection, we derive the expressions for both displacement and strain for different relaxation scenarios. We assume that the material viscoelasticity can be described by the Kelvin–Voigt model, which is a lumped element model comprising a spring and a dashpot in parallel (as described on page 87 of Ref. 34). The constitutive equations then read

$$\begin{cases} \rho \dfrac{\partial^2 \mathbf{u}}{\partial t^2} = \nabla \cdot \sigma, \\ \sigma = \mathbf{C}\varepsilon + \eta \dfrac{\partial \varepsilon}{\partial t}, \end{cases} \tag{14}$$

where $\mathbf{u}$ (m) is the displacement field, σ (Pa) is the stress tensor, $\mathbf{C}$ (Pa) is the stiffness matrix tensor, and η (Pa s) is the viscosity tensor. The strain ε can be cast in the form

$$\varepsilon = \nabla_S \mathbf{u} - \gamma_M \Delta T, \tag{15}$$

where $\nabla_S \mathbf{u} = \frac{\nabla \mathbf{u} + \nabla^T \mathbf{u}}{2}$, γ_M (K^{-1}) is the matrix of linear expansion, and ΔT is the temperature variation.[35] This approach is in agreement with the Green–Lindsay theory for thermoviscoelastic media.[36,37]

We write the viscoelastic tensor as $\eta = \tau_\eta \mathbf{C}$,[38] where τ_η is addressed in the literature as the *mechanical relaxation parameter of the viscoelastic solid*.[36] We pinpoint that τ_η should not be confused with the viscoelastic damping time, the latter actually being a decreasing function of the parameter τ_η. Furthermore, we assume the medium to be homogeneous and isotropic. Upon these assumptions, the equation ruling the displacement field reads

$$\frac{\partial^2 u_x}{\partial t^2} = c_L^2 \left(1 + \tau_\eta \frac{\partial}{\partial t}\right) \frac{\partial^2 u_x}{\partial x^2} - (3c_L^2 - 4c_T^2)\gamma \left(1 + \tau_\eta \frac{\partial}{\partial t}\right) \frac{\partial T}{\partial x}, \tag{16}$$

where $c_L = \sqrt{(\lambda + 2\mu)/\rho}$ and $c_T = \sqrt{\mu/\rho}$ are the longitudinal and transverse velocities (m/s), with λ (Pa) and μ (Pa) being the two Lamé coefficients and γ (K^{-1}) being the linear thermal expansion coefficient.

Performing temporal Fourier transform, Eq. (16) reads

$$\begin{aligned} -\omega^2 \tilde{u}_x &= c_L^2 (1 + i\omega\tau_\eta) \frac{\partial^2 \tilde{u}_x}{\partial x^2} \\ &- \left(3c_L^2 - 4c_T^2\right)(1 + i\omega\tau_\eta)\gamma \frac{\partial \tilde{T}}{\partial x}. \end{aligned} \tag{17}$$

By defining

$$c^2(\omega) = c_L^2 (1 + i\omega\tau_\eta) \tag{18}$$

and

$$\xi = 3 - 4\frac{c_T^2}{c_L^2}, \tag{19}$$

Eq. (17) is cast in the more compact form

$$\frac{\partial^2 \tilde{u}_x}{\partial x^2} + \frac{\omega^2}{c^2(\omega)} \tilde{u}_x = \xi\gamma \frac{\partial \tilde{T}}{\partial x}. \tag{20}$$

In order to calculate the displacement triggered by the TTG excitation, we use the solution for the temperature in the frequency domain previously derived in Eq. (4),

$$\frac{\partial^2 \tilde{u}_x}{\partial x^2} + \frac{\omega^2}{c^2(\omega)} \tilde{u}_x = Z(\omega) \sin(qx), \tag{21}$$

where

$$Z(\omega) = -\frac{qQ_0\xi\gamma}{2i\rho C(\omega - i\alpha q^2)}. \tag{22}$$

The general solution of Eq. (21) is $\tilde{u}(x,\omega) = z(x,\omega) + z_p(x,\omega)$, where $z_p(x,\omega)$ is a particular solution of Eq. (21), while $z(x,\omega)$ is the solution of the associated homogeneous differential equation. It can be shown that

$$z_p(x,\omega) = \frac{Z(\omega)c^2(\omega)}{\omega^2 - q^2c^2(\omega)} \sin(qx) \tag{23}$$

is a particular solution of Eq. (21).

In order to have the system at rest before the excitation [i.e., $u(x,t) = 0$ and $\frac{du}{dt}(x,t) = 0$ for negative times] and avoid the divergence of the displacement at infinity, we must have $z(x,\omega) = 0\ \forall\omega$. Hence, the final solution is

$$\tilde{u}(x,\omega) = z_p(x,\omega) = \frac{Z(\omega)c^2(\omega)}{\omega^2 - q^2c^2(\omega)} \sin(qx). \tag{24}$$

Upon insertion of the expressions for $Z(\omega)$, ξ, and $c(\omega)$, Eq. (24) reads

$$\tilde{u}(x,\omega) = -\frac{qQ_0\gamma\left(3c_L^2 - 4c_T^2\right)(1 + i\omega\tau_\eta)}{2i\rho C(\omega - i\alpha q^2)(\omega - \omega_3)(\omega - \omega_4)} \sin(qx), \tag{25}$$

where

$$\omega_3 = i\frac{q^2}{2}\left[c_L^2\tau_\eta - \sqrt{c_L^4\tau_\eta^2 - \frac{4\rho}{q^2}c_L^2}\right] \tag{26}$$

and

$$\omega_4 = i\frac{q^2}{2}\left[c_L^2\tau_\eta + \sqrt{c_L^4\tau_\eta^2 - \frac{4\rho}{q^2}c_L^2}\right]. \tag{27}$$

The angular frequencies ω_3 and ω_4 contain the acoustic parameters, and they describe the damped oscillation part of the signal.

B. ISTS response in the case of frequency-independent specific heat and thermal expansion

If the specific heat and the thermal expansion coefficient do not depend on the frequency, we can apply inverse Fourier transform to Eq. (25) (see Sec. I of the supplementary material) to obtain the time domain expression for the displacement,

$$\begin{aligned} u(x,t) = & -\frac{qQ_0\gamma}{2\rho C}\sin(qx)\left(3c_L^2-4c_T^2\right) \\ & \times\left\{\frac{1-\alpha q^2\tau_\eta}{(i\alpha q^2-\omega_3)(i\alpha q^2-\omega_4)}\exp\left(-\alpha q^2 t\right)\right. \\ & +\frac{1+i\omega_3\tau_\eta}{(\omega_3-i\alpha q^2)(\omega_3-\omega_4)}\exp(i\omega_3 t) \\ & \left.+\frac{1+i\omega_4\tau_\eta}{(\omega_4-i\alpha q^2)(\omega_4-\omega_3)}\exp(i\omega_4 t)\right\}\theta(t). \end{aligned} \tag{28}$$

C. ISTS response in the case of frequency-dependent specific heat and thermal expansion described by the Debye model

In this section, we assume that the specific heat depends on the frequency according to the Debye model, in analogy with Subsection II B 1. Hence, we substitute Eq. (6) into Eq. (25), obtaining

$$\tilde{u}(x,\omega) = -\frac{qQ_0\gamma\left(3c_L^2-4c_T^2\right)(1+i\omega\tau_\eta)(\omega-i\omega_C)}{2i\rho C_\infty(\omega-\omega_1)(\omega-\omega_2)(\omega-\omega_3)(\omega-\omega_4)}\sin(qx), \tag{29}$$

where ω_1 and ω_2 are defined in Eqs. (9) and (10), respectively. We also assume the linear thermal expansion coefficient to be frequency-dependent according to the Debye expression,

$$\gamma(\omega) = \gamma_\infty + \frac{\Delta\gamma}{1+i\omega\tau_\gamma} = \gamma_\infty + \frac{\Delta\gamma}{1+i\frac{\omega}{\omega_\gamma}}, \tag{30}$$

where γ_∞ and $\Delta\gamma$ represent the infinite frequency and an additional relaxation contribution (occurring at a low frequency) to the thermal expansion, respectively, with $\omega_\gamma = \tau_\gamma^{-1}$ being its associated relaxation frequency.

For the sake of keeping the analytics simple, and given that the focus of this work is on the thermal expansion portion of the signal rather than on the superposed acoustic part, in the following, we neglect the frequency and temperature dependence of both the elastic moduli and the density.[3–6]

With this choice, the equation to be solved reduces to

$$\frac{\partial^2\tilde{u}_x}{\partial x^2} + \frac{\omega^2}{c^2(\omega)}\tilde{u}_x = \xi\left(\gamma_\infty + \frac{\Delta\gamma}{1+i\frac{\omega}{\omega_\gamma}}\right)\frac{\partial\tilde{T}}{\partial x}. \tag{31}$$

The expression for $\gamma(\omega)$ can be rewritten as

$$\gamma(\omega) = \gamma_\infty\frac{\omega-i\omega_\gamma\left(1+\frac{\Delta\gamma}{\gamma_\infty}\right)}{\omega-i\omega_\gamma} = \gamma_\infty\frac{\omega-\omega_6}{\omega-\omega_5}, \tag{32}$$

where

$$\omega_5 = i\omega_\gamma \tag{33}$$

and

$$\omega_6 = i\omega_\gamma\left(1+\frac{\Delta\gamma}{\gamma_\infty}\right). \tag{34}$$

Substituting Eq. (32) into Eq. (29), we get

$$\tilde{u}_x(x,\omega) = -\frac{qQ_0\gamma_\infty\left(3c_L^2-4c_T^2\right)(1+i\omega\tau_\eta)(\omega-i\omega_C)(\omega-\omega_6)}{2i\rho C_\infty\prod_{j=1}^{5}(\omega-\omega_j)}\sin(qx). \tag{35}$$

By inverse Fourier transforming the latter expression, we obtain the solution for the displacement in the time domain,

$$\begin{aligned} u_x(x,t) = & -\left[\frac{qQ_0\gamma_\infty\sin(qx)}{2\rho C_\infty}\right]\left(3c_L^2-4c_T^2\right) \\ & \times\sum_{l=1}^{5}\left\{(1+i\omega_l\tau_\eta)(\omega_l-i\omega_C)(\omega_l-\omega_6)\right. \\ & \left.\times\left(\prod_{\substack{j=1\\ j\neq l}}^{5}\frac{1}{\omega_l-\omega_j}\right)\exp(i\omega_l t)\right\}\theta(t). \end{aligned} \tag{36}$$

The latter expression contains the sum of five time-dependent exponential functions. The exponentials containing angular frequencies ω_1 and ω_2 are related to the heat capacity thermal relaxation, whereas the exponentials ruled by ω_3 and ω_4 describe the acoustic part of the signal. Finally, the term $\exp(i\omega_5 t)$ accounts for the relaxation of the thermal expansion coefficient.

The ISTS signal $U_{ISTS}(t)$ is proportional to the relative density variation $\Delta\rho/\rho$, which, in turn, is proportional to the strain grating amplitude.[32,39] The strain equals the spatial derivative of the 1D displacement pattern. Hence, the ISTS signal, derived from Eq. (36), reads

$$U_{ISTS}(t) \propto \max_x\left[\frac{\partial u_x(x,t)}{\partial x}\right]. \tag{37}$$

In the following, we fit the experimental ISTS signal with the expression reported on the right-hand-side of Eq. (37). The fitting parameters are c_L, τ_η, C_∞, $\Delta C/C_\infty$, ω_C, $\Delta\gamma/\gamma_\infty$, and ω_γ, in total seven variables. The density ρ and thermal conductivity κ_T are treated as non-relaxing quantities,[20] with constant values of 1260 kg/m^3 and 0.28 W m^{-1} K^{-1}, respectively, taken from the literature.[6,40] The values of the multiplicative pre-factor in the expression, and the individual parameters therein, are not retrievable from fitting.

D. ISTS response in the case of frequency-dependent specific heat and thermal expansion described by the Havriliak–Negami model

In the HN scenario for the thermal expansion response, we have

$$\gamma(\omega) = \gamma_\infty + \frac{\Delta\gamma}{\left[1 + (i\omega\tau_\gamma)^{a_\gamma}\right]^{b_\gamma}} = \gamma_\infty + \frac{\Delta\gamma}{\left[1 + \left(i\frac{\omega}{\omega_\gamma}\right)^{a_\gamma}\right]^{b_\gamma}}, \tag{38}$$

with a_γ and b_γ being two additional parameters. Casting the specific heat per unit mass in the HN form, as described in Subsection II B 2, we obtain

$$\tilde{u}(x,\omega) = -\frac{qQ_0\gamma_\infty\left(3c_L^2 - 4c_T^2\right)(1 + i\omega\tau_\eta)\left[\omega_C^{a_C} + (i\omega)^{a_C}\right]^{b_C}\left\{\left[\omega_\gamma^{a_\gamma} + (i\omega)^{a_\gamma}\right]^{b_\gamma} + \frac{\Delta\gamma}{\gamma_\infty}\omega_\gamma^{a_\gamma b_\gamma}\right\}\sin(qx)}{2i\rho C_\infty\left\{\omega\left[\omega_C^{a_C} + (i\omega)^{a_C}\right]^{b_C} + \frac{\Delta C}{C_\infty}\omega\omega_C^{a_C b_C} - i\alpha_\infty q^2\left[\omega_C^{a_C} + (i\omega)^{a_C}\right]^{b_C}\right\}(\omega - \omega_3)(\omega - \omega_4)\left[\omega_\gamma^{a_\gamma} + (i\omega)^{a_\gamma}\right]^{b_\gamma}}. \tag{39}$$

As we anticipated in Sec. II B 2, since the exponents a_C, a_γ, b_C, and b_γ may be non-integer, working out Fourier transform of expression (39) analytically is rather involved. For this reason, in the case of the HN model, it is more convenient to apply the numerical Fourier transform to the experimental ISTS signal and then fitting it with Eq. (39). Analogously, we obtain the displacement in the time domain by applying the numerical Fourier's inverse transform to Eq. (39).

Compared to the Debye-based ISTS model, the fitting involves four additional parameters, i.e., a_C, a_γ, b_C, and b_γ.

The detailed derivation of the disentangled model has been presented above. The two key questions motivating the current work are (i) whether the DE model based mathematical description of ISTS signals, in which the heat to temperature and temperature to volume (or equivalently, temperature to density) responses are disentangled, adequately fits the experimental signals, and (ii) if it is feasible to separately extract the relaxation parameters of the specific heat and the thermal expansion.

IV. COMPARISON WITH THE STRETCHED EXPONENTIAL MODEL

Given the fact that the existing stretched exponential (SE) model has been widely used to describe/fit ISTS signals of glass-forming liquids, e.g., salol[12,13,18] and glycerol,[14] the first step, to tackle the above-mentioned questions, is to verify how well SE-based signals can be fitted by the disentangled (DE) model, accounting for relaxation in the frame of either Debye or HN theory. Otherwise stated, we should verify how well the DE model can describe/reproduce an ISTS waveform generated by the SE model.

A. Constituents of the SE model

The SE model is given by Eq. (40), where the first term is associated with the thermal diffusion (Γ_H is the thermal decay rate), while the second one accounts for the acoustics ($\omega_A = 2\pi f_A$ is the acoustic oscillation frequency and Γ_A is the acoustic damping rate). The use of a stretched exponential term—also known as Kohlrausch–Williams–Watts (KWW)—was inspired by other response functions in the physics of supercooled liquids. It was introduced as a remedy to the fact that the thermal expansion cannot be fitted by a simple exponential; Γ_R is the structural relaxation rate, and $0 < \beta \leq 1$ is the stretching exponent. The coefficients A and B account for the weights of each term contributing to the total ISTS signal,[41]

$$I(t) = (A + B)\exp(-\Gamma_H t) - A\exp(-\Gamma_A t)\cos(\omega_A t) - B\exp\left[-(\Gamma_R t)^\beta\right]. \tag{40}$$

B. ISTS waveforms of glycerol simulated by the SE model and their reproduction with the DE model

In order to mathematically inspect the compatibility between the newly developed DE model and the existing SE model, we exploited the DE model to fit ISTS signals generated by SE model for several temperature–wavenumber combinations.

The values for glycerol reported by Paolucci and Nelson[14] are recalled in Table I and were used to reproduce the experimental ISTS signals reported in the literature [see Fig. 1 (black curves)]. Three cases are considered in Fig. 1: In panels a and b, the ISTS of glycerol is reported for the two grating wavenumbers $q = 3.05 \times 10^5$ and $q = 1.036 \times 10^6$ m^{-1}, respectively, at the same temperature $T_0 = 250$ K (i.e., cases Nos. 1 and 2 in Table I, respectively). Panel (c) reports

TABLE I. Material parameters reported by Paolucci and Nelson[14] based on the SE model fits of ISTS signals in supercooled glycerol.

Case	No. 1	No. 2	No. 3	No. 4
T_0 (K)	250	250	230	230
q (m^{-1})	3.05×10^5	1.036×10^6	3.05×10^5	1.036×10^6
Γ_H (s^{-1})[a]	1.14×10^4	1.33×10^5	1.38×10^4	1.59×10^5
Γ_A (s^{-1})[b]	3.5×10^7	8.5×10^7	2.0×10^6	2.5×10^6
f_A (Hz)[c]	1.56×10^8	5.28×10^8	1.64×10^8	5.56×10^8
β[d]	0.6	0.6	0.6	0.6
Γ_R (s^{-1})[e]	5.5×10^6	5.5×10^6	1.1×10^5	1.1×10^5
B/A[f]	2.03	2.03	2.03	2.03

[a]The thermal decay rate was estimated to be $\Gamma_H = \kappa_T q^2/(\rho C_{eff})$, where $\kappa_T = 0.28$ W/m K, $\rho = 1260$ kg/m^3, and $C_{eff} = 1800$ J/(kg K) (for $T_0 = 250$ K) and $C_{eff} = 1500$ J/(kg K) (for $T_0 = 230$ K). The estimation of C_{eff} from Ref. 14 turns outs to be unpractical; hence, the values of Γ_H are somewhat arbitrary, leading to unrealistic fitting values for C_∞.

[b]The acoustic damping rate was taken from Fig. 3 of Ref. 14.

[c]The acoustic oscillation frequency was obtained as the product between q and the speed of sound reported in Fig. 3 of Ref. 14.

[d]The stretch exponent was taken from Fig. 5 of Ref. 14.

[e]The structural relaxation rate was obtained as $\Gamma_R = \Gamma(1/\beta)/(\langle\tau\rangle\beta)$, where Γ is the gamma function, and $\langle\tau\rangle$ was taken from Fig. 4 of Ref. 14.

[f]The ratio between the coefficients B and A was calculated as $B/A = f/(1 - f)$, where $f = 0.67$ is the Debye–Waller factor taken from Fig. 7 of Ref. 14.

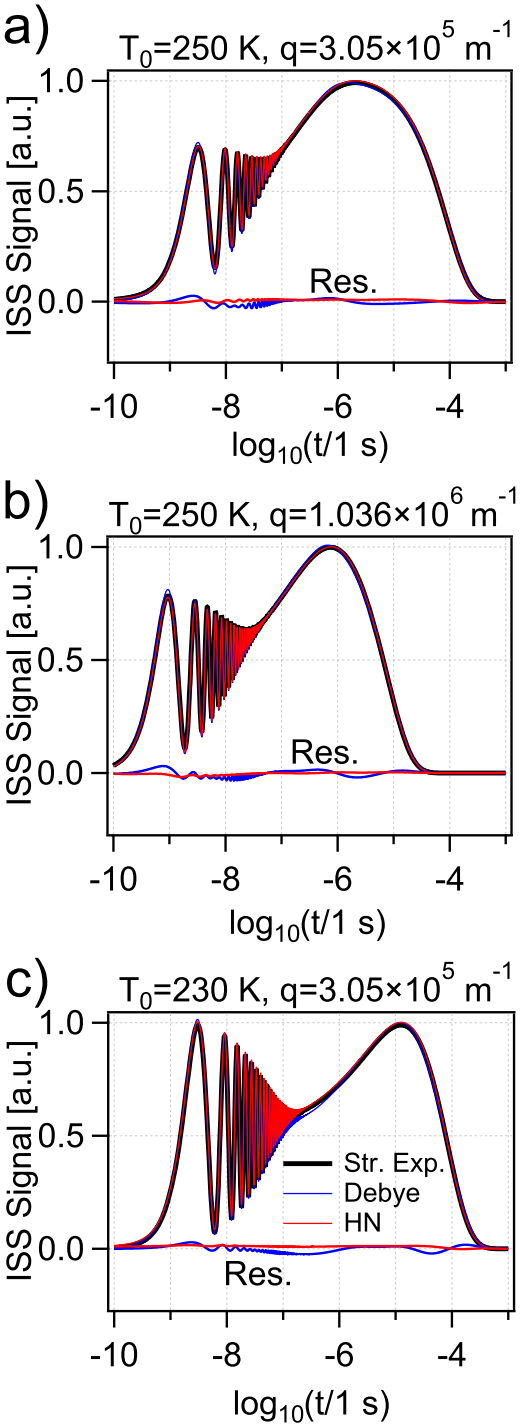

FIG. 1. Plot of ISTS waveforms generated by the SE model (black curves), and their reproduction/fit with the Debye model (blue curves) and the HN model (red curves), for different temperature–wavenumber combinations, based on the parameters listed in Table I. The small fitting residues (fitting curve minus SE model curve) indicate that the Debye-based model is adequate. Thanks to the two additional model parameters, the HN model is fitting/reproducing even better. In each panel, all the curves are normalized to the maximum of the ISTS signal.

the ISTS signal for a lower temperature of $T_0 = 230$ K and for the shortest grating wave vector available, i.e., $q = 3.05 \times 10^5$ m^{-1} (case No. 3 in Table I). For each panel, the value of the coefficient A was chosen in order to have the maximum of the ISTS signal normalized to 1.

We have fitted the black curves in Fig. 1 with the corresponding DE model expressions (blue curves: Debye, red curves: HN). The obtained fitting parameters are reported in Table II. The C_∞ values are not realistic due to the arbitrarity in the estimation of the thermal decay rate from Ref. 14 in Table I. Neither is the relaxation strength of the thermal expansion. The HN coefficients are somewhat reasonable (except case 3), around 0.88 and 0.60, corresponding to a stretched exponential β of 0.60.[42] The fitting was carried out by implementing a most-squares fitting (MSF) protocol[43,44] to search for the minimum of the cost function, defined as the sum of the squared residuals (SSR). MSF is advantageous over the commonly used least-squares fitting (LSF) as it accounts for the co-variance of the multiple fitting variables, namely, different combinations of fitting parameters yielding a statistically indistinguishable cost function value SSR. The procedures of the MSF and LSF fitting are illustrated in Sec. III of the supplementary material. As can be seen in Fig. 1, both models fit very well, with the residues of the HN model being the smallest (negligible), owing to the additional two fitting parameters. In addition, it appears that the SE model displays a nonphysical change of sign for the ISTS signal (e.g., case No. 4), when the characteristic relaxation time, determined by the DC temperature, is longer than the thermal diffusion time (determined by the wavenumber). This feature is lacking at high temperatures and for long grating periodicity since the relaxation dynamics is always completed before the thermal decay. The model here developed solves this pitfall, with no sign change being introduced. We rationalize this pitfall in Sec. II of the supplementary material.

TABLE II. Parameter values obtained by fitting the SE model ISTS signals reported in Fig. 1 with the expressions obtained in the framework of Debye and HN behavior. The choice of the fitting model does not influence the values obtained for acoustic parameters c_L and τ_η.

Case	No. 1	No. 2	No. 3
C_∞ Debye (J/kg K)	452	460	360
C_∞ HN (J/kg K)	500	500	390
C_0 Debye (J/kg K)	1837	1882	1645
C_0 HN (J/kg K)	1777	1777	1345
$\Delta\gamma/\gamma_\infty$ D	10	10	10
$\Delta\gamma/\gamma_\infty$ HN	9.4	9.4	9.8
f_C (Hz) Debye	8.12×10^5	1.05×10^6	3.18×10^4
f_C (Hz) HN	5.57×10^5	5.57×10^5	2.38×10^5
f_γ (Hz) Debye	5.07×10^5	6.49×10^5	2.41×10^4
f_γ (Hz) HN	3.61×10^5	3.61×10^5	6.02×10^3
a_c HN	0.89	0.89	0.54
b_c HN	0.52	0.52	0.78
a_γ HN	0.95	0.95	0.75
b_γ HN	0.68	0.68	0.55
c_L (m/s)	3200	3200	3369
τ_η (ps)	88	18	41

Summarizing, the DE model developed in this work can adequately reproduce/describe the SE model-generated ISTS signals. The residuals are negligible and would be smeared out if experimental noise was present. The SE model has the advantage of being simple. It assumes that the relaxation for specific heat and thermal expansion occurs on the same time scale and connects their contribution to the ISTS signal via a single stretched exponential. The proposed DE model is more complicated, but it explicitly treats the two quantities as independent relaxation dynamics.

V. EXPERIMENTAL RESULTS AND DISCUSSION

The disentangled models are conceived to enable the extraction of specific heat and thermal expansion relaxation from ISTS signals, in addition to the acousto-mechanical relaxation. With this aim in mind, this section reports on **(A)** the experimental ISTS signals of glycerol under supercooling conditions and their best fit with three models, namely, the two versions of the disentangled model developed in this work (Debye and HN) and the SE model; **(B)** analysis of the experimental and fitting uncertainty; **(C)** the acousto-mechanical relaxation; **(D)** the relaxation of C and γ, relaxation strength and relaxation frequency over a frequency span ranging all the way to the sub-100 MHz; and **(E)** comparison between mechanical and thermal relaxation.

A. Experimental ISTS signals and best fitting

In the following, an experimental study of the ISTS response of glycerol (>99.0% purity) under supercooling is presented and analyzed at the light of the above-developed theoretical frame. A heterodyne-detected transient grating (HD-TG) setup was deployed for the experiment.

Figure 2 shows the scheme of the setup. A ps pump laser pulse at 1064 nm (shown in red) is diffracted by a transmission phase mask (PM) into two first diffraction orders, namely, ±1 orders. The two are then recombined via a two-lens ($4f$) imaging system into the bulk of the sample. The sample is accommodated in a liquid nitrogen optical cryostat (OC). Beams interference forms a transient spatially periodic light pattern, ultimately resulting, via the thermoelastic effect, in a transient density grating of periodicity d. The optical absorption coefficient of pure glycerol at 1064 nm[45] is about 0.26 cm^{-1}.The pulse energy and repetition rate of the pump laser were 0.5 mJ and 1 kHz, respectively, corresponding to an average excitation power of 500 mW.

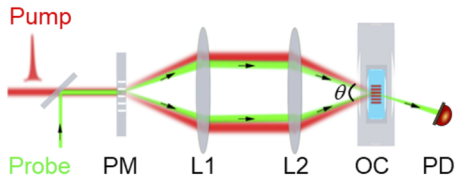

FIG. 2. Scheme of the experimental setup based on the heterodyne-detected transient grating technique. A spatially periodical laser pattern from a pulsed pump laser (red) is formed in the sample bulk to create thermoelastic transients, which is detected by a coaxially aligned probe laser (green and arrows). In the scheme, we sketch the phase mask (PM), the lenses (L1 and L2), the optical cryostat (OC), and the photodetector (PD).

For a given light wavelength λ, one can tune the spacing of the excitation pattern by varying the intersecting angle of the two beams θ, namely, via $d = \lambda/(2n)\sin(\theta/2)$ with n being the optical refractive index of the sample medium. In this setup, the θ-tuning is implemented by translating a phase mask (PM) array containing multiple PMs of varying periodicities.[46] Alternatively, one can also rotate the PM to realize the θ-tuning.[47] The detection of ISTS takes advantage of the optical heterodyne scheme,[48] in which the probe beam from a continuous wave (CW) laser at a wavelength of 532 nm (shown in green with black arrows in Fig. 2) is aligned to be coaxial with the pump beam. Both beams are sent to the PM and diffracted into excitation and probe/reference beam pairs. This heterodyne scheme has been widely used in the field for studying optical transparent or weakly absorbing liquids[10,49,50] owing to its high sensitivity. In our experiments, measurements were performed from 320 to 200 K with a step of 1 K, under the excitation of three different gratings with d of 10, 14, and 20 μm.

Figure 3(a) shows the recorded ISTS waveform datasets. As the DC temperature decreases, the oscillation frequency of the acoustic ripples evident at short times shifts from low to high, i.e., from 60 to 350 MHz, with the attenuation reaching a maximum around 280 K. This observation reflects the solidification of the sample, which undergoes a transition from liquid-like to glassy-like, and solid-like due to reduced molecular mobility.[51] The overshoot-like response is noteworthy, spanning from the start of the signal (bluish region), where it overlaps with the acoustic oscillations and fast part of thermal expansion, until later times (reddish region), when it is quenched by the thermal diffusion dominated part (bluish tail). This process is the manifestation of the relaxation of specific heat and thermal expansion coefficient, which are strongly (quasi exponentially) temperature dependent.

B. Measurement uncertainty and fitting uncertainty

We performed a comparative fitting analysis of the acquired ISTS datasets via the two DE models (i.e., using the Debye and HN relaxation functions) and via the SE model. The best-fitting results are summarized in Figs. 3(b)–3(d) and are also available in the online Movies 1–3 in the supplementary material. Satisfactory fitting quality is achieved for all temperatures and grating periods, confirming again the reliability of the models developed in this work. Before presenting the obtained relaxation results, we shortly discuss the sources of uncertainty from both the measurements and data processing. The following uncertainties are of importance:

(i) A possible DC temperature offset at the measurement location(crossing region of laser beams) with respect to the measured temperature, caused by the photothermal heating that is driving the ISTS signal response. Measurements of the DC temperature of the sample were done by a calibrated platinum (Pt) resistor immersed in the glycerol sample, at a location (about 5 mm) away from the laser beams. The calibration uncertainty of the Pt resistor was 0.1 K. The effective uncertainty on the DC temperature values is larger, as the photothermal heating not only generates a transient temperature

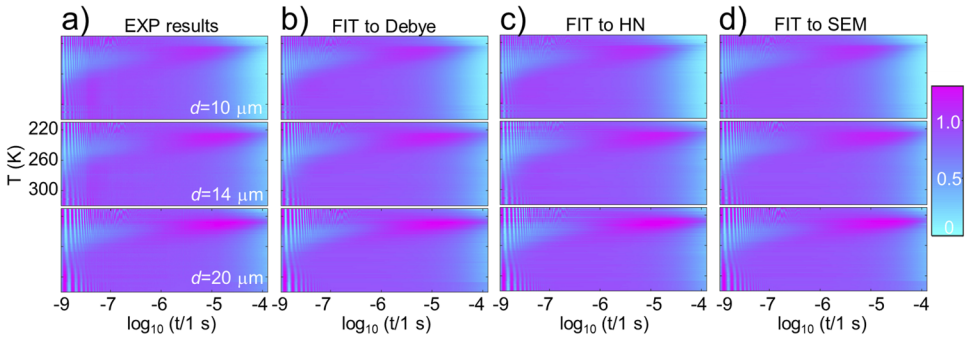

FIG. 3. (a) Experimental ISTS signal (color scale, arbitrary units) of supercooled glycerol over a broad temperature (vertical axis) and time window (horizontal axis). The grating size is 10 μm (top), 14 μm (central), and 20 μm (bottom). [(b)–(d)] Best fit based on the Debye, HN, and SE models, respectively. The graph presents an overview of the large amount of experimental data and their best fitting (total 1080 traces and fittings). A full presentation of the best fit of all waveforms is shown in the movies in the supplementary material, from which one can visualize/compare in detail the fitting by the three models for every individual temperature and grating.

change but also a shift of the temperature baseline. In order to determine the local temperature rise in the laser beam crossing region where the signal was generated with respect to the Pt resistor location, we have measured the long-term accumulated laser heating in a somewhat similar system, i.e., copper chloride (CuCl2)–Rhodamine B dyed glycerol, 3.8 cm^{-1}. This material was impulsively heated at 1064 nm with a similar average power input, 650 mW, as in the ISTS experiment. The DC temperature drift in CuCl2–RhB dyed glycerol, measured by using fluorescence based thermometry,[52] was found to be about 15 K. By taking into account a lower optical absorption coefficient of 0.26 cm^{-1} at 1064 nm in pure glycerol as used in the ISTS setup, the DC temperature offset in pure glycerol can be estimated to be 15 K $\times(0.26/3.8\ cm^{-1}) \times (500/650\ mW) = 0.8$ K. We consider this to be representative for the uncertainty on the DC temperature values reported in this work.

(ii) Errors on the fitting parameters. Taking into account the relaxation of both specific heat and thermal expansion in the ISTS response almost unavoidably leads to the introduction of additional fitting parameters. The fitting involves in total seven parameters when using the Debye-based ISTS model, the same as the SE model [Eq. (40)]. Four additional parameters appear when using the HN-based ISTS model. We performed the fitting from high to low temperatures in an iterative way, with the best-fitting results from the previous temperature as the initial guess for the fitting of the current one. The fitting of the highest temperature 320 K does not necessarily require an accurate initial guess, as glycerol acts like a non-relaxing material at that temperature. In this case, C_0 and two acoustic parameters can be easily fitted because the thermal diffusion is dominated only by C_0. Furthermore, the acoustic oscillations are both well defined by the known grating spacing and by these parameters only, without covariance with other parameters. The initial-guessed relaxation time for C and γ could be an arbitrarily large number, e.g., 0.5 ns, which did not influence the fitting. Our confidence in the fitted values was further enhanced by making use of most-squares error (MSE) analysis,[43,44] i.e., by scanning each fitting variable around the best-fitting value in a broad range 10%–200% and performing a new round of fitting with all the rest variables as fitting parameters. Not only this protocol allows us to evaluate the margin of fitting uncertainty that takes into account the fitting co-variance but the refined additional cost function minimizations also ensure that the global minimum of the cost function is reached in the minimization of the fitting process. For this reason, the fitting is stable and the results are independent of the initial guess. A few examples of the MSE analysis are given in the supplementary material.

ISTS signals are information-rich, providing access to the mechanical and thermal relaxation dynamics in a single waveform, which will be discussed in the following.

C. Relaxation of longitudinal speed of sound

The acoustic ripples at the beginning of the ISTS waveforms allow us to assess the temperature evolution of the longitudinal sound velocity and the acousto-mechanical relaxation. Specifically, by fitting the experimental traces with our models, for every temperature and light grating, we retrieve c_L and τ_η. Upon insertion of these parameters into Eq. (18), we calculate the complex sound velocity at the acoustic frequency imposed by the grating $\omega_a = 2\pi c_L/d$. Figure 4 shows the obtained complex sound velocity of supercooled glycerol, as determined at three grating periodicities, at different temperatures. The real part of c (top panel) increases upon cooling because of the stiffening of the liquid. The imaginary part of c (bottom panel) reaches a maximum around 280 K, where the structural relaxation time scale overlaps with the acoustic one. The results are in good agreement with those reported in Ref. 14. It is interesting to notice that both the real and imaginary part undergo a transition around 280 K. This evidence is traceable to the strong coupling between the acoustic motion and the network structural changes, taking place when $1/f_A$ is of the order of the structural relaxation time. This feature provides a mean to study the mechanical relaxation by performing measurements at numerous grating periodicities,[4,5]

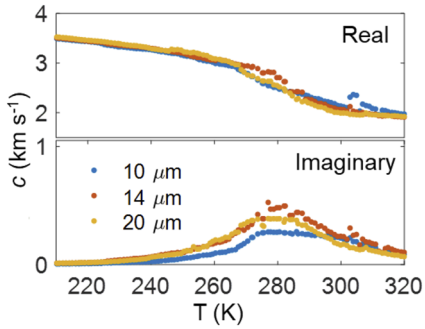

FIG. 4. Temperature-dependent complex longitudinal sound velocity (c) determined with the three gratings. The top (bottom) panel corresponds to the real (imaginary) part of c.

complementing traditional rheological[3] and ultrasonic spectroscopy (US).[53,54]

Using the ISTS technique to investigate the mechanical relaxation has been well established by Keith Nelson and co-workers (e.g., Ref. 14). The approach requires one to carry out measurements at different grating spacings, from which one can establish a mechanical (frequency) spectrum, as illustrated in Ref. 4. The asymmetric shape of the spectrum can then be investigated, e.g., via HN or power-law models, to identify the non-exponential behavior of mechanical relaxation, like in other types of frequency-resolved spectroscopies, e.g., dielectric spectroscopy (DS). In principle, we could also take into account the acoustic relaxation in the modeling, in analogy to what we have done for the specific heat and thermal expansion. From a practical point of view, however, this would make the analytic calculations impractically complicated and it would not yield additional information. This is because the bandwidth and quality of the acoustic part of the signals are not sufficient to discriminate between Debye or more complex non-exponential types of behaviors.

Our choice to condense the sound propagation to two frequency-independent numbers in fitting the individual signals implicitly implies that exponential relaxation was assumed. This has led to satisfactory fits of the acoustic signals, like using a damped sinusoidal function in Eq. (40). No attempt was made to establish whether the assumption of exponential behavior was adequate. The reason for the good fitting quality in spite of the *ad hoc* assumption of frequency-independent mechanics lies in the narrow bandwidth of most of the acquired ISTS signals, implying that their spectrum only covers a narrow region of the acoustic dispersion curve. Over this narrow region, the acoustic parameters do not vary very much. Moreover, for most of the signals, the high-frequency acoustic peak in the signal spectrum is well separated from the low-frequency thermal expansion part of the spectrum so that the two responses are decoupled. Only for the signals where the acoustic part is strongly damped, indicating mechanical coupling with the relaxation, the acoustic peak in the spectrum is wide. However, the tails of the spectral peak are small in the frequency range where they overlap with the thermal expansion part of the spectrum so that the details of the (fit of the) acoustic signal do not significantly affect the fit of the thermal expansion. In addition, for strongly damped acoustic signals whose spectrum covers a wide range of the acoustic dispersion curve, the signal-to-noise ratio of the spectral peak is not sufficient to make conclusions concerning the details of the relaxation process (Debye model or more complicated model).

D. Relaxation of specific heat C and thermal expansion coefficient γ

In addition to the mechanical relaxation dynamics, the models developed in this work allow us to individually and simultaneously retrieve both the specific heat capacity C and the thermal expansion coefficient γ relaxations. In the following, we focus on the case $d = 14$ μm, analyzed in the frame of Debye model, the other cases yielding the same conclusions.

Figure 5(a) shows the low-frequency response of C (left axis, red) and γ (right axis, blue). Panel (b) displays the fitted ratio $\Delta C/C_\infty$ (left axis, red) and $\Delta\gamma/\gamma_\infty$ (right axis, blue) at different temperatures. The fitting uncertainties were determined by the most-squares error analysis. Very large fitting uncertainties were found for $T < 230$ K and $T > 260$ K, which is related with the experimentally accessible time window. The fast and slow limit is about 1 ns and 100 μs, determined by the optical detection bandwidth of the setup (1 GHz) and by the thermal diffusion driven decay of the signal, respectively. The relaxation process is then either too slow (when $T < 230$ K) or too fast to detect (when $T > 260$ K). Accessing the physics at lower temperatures requires adopting larger grating spacing or alternative beam shaping.[55] Small fitting errors were found between 230 and 260 K. Within the margin of uncertainties, no temperature dependence is observed for both the low-frequency limit response and the ratio, as can be seen in Fig. 5.

Table III reports the low/high-frequency limit values for $C(\omega)$ and $\gamma(\omega)$ and, for comparison, available values from the literature. Our results, represented by the average values between 230 and 260 K, match well the values for specific heat from differential scanning calorimetry (DSC),[57] specific heat capacity from 3ω,[19,56] and photopyroelectric spectroscopy (PPE).[20,21] respectively. The thermal expansion results are in good agreement with the values retrieved

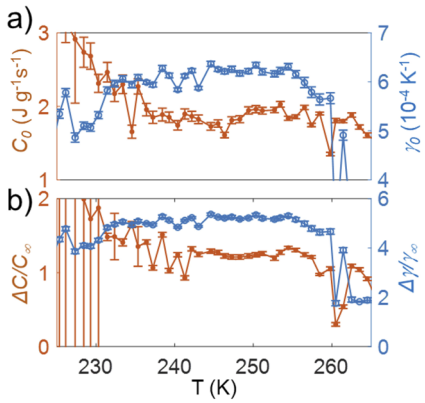

FIG. 5. (a) Low-frequency limit of C (left axis, red) and γ (right axis, blue) vs temperatures. (b) Relative ratio of each relaxation quantity, $\Delta C/C_0$ (left axis, red) and $\Delta\gamma/\gamma_0$ (right axis, blue). The data were obtained from the fit in the frame of the Debye model and for $d = 14$ μm.

TABLE III. Low-frequency and high-frequency limit of the average relaxing quantity C and γ and comparison with results in the literature obtained with 3ω, differential scanning calorimetry (DSC), and photopyroelectric spectroscopy (PPE). In 3ω and PPE, one measures thermal effusivity (e), from which $C(\omega)$ may be indirectly obtained via $e^2 = C\kappa_T$, with κ_T being the thermal conductivity. To perform the conversion, we used $\kappa_T = 0.29$ W m^{-1} K^{-1}.

	ISTS fit	3ω[19,56]	PPE[20,21]	DSC[57]
C_0 (J kg^{-1} K^{-1})	1980 ± 160	2071	2100	2000
C_∞ (J kg^{-1} K^{-1})	910 ± 150	1070	1180	1000
R_S	0.5 ± 0.1	0.48	0.44	0.5
	ISTS fit	Dilatometer[6]		
γ_0 (10^{-4} K^{-1})	5.5 ± 0.7	5		
γ_∞ (10^{-4} K^{-1})	⋯	1		
R_S	0.81 ± 0.04	0.8		

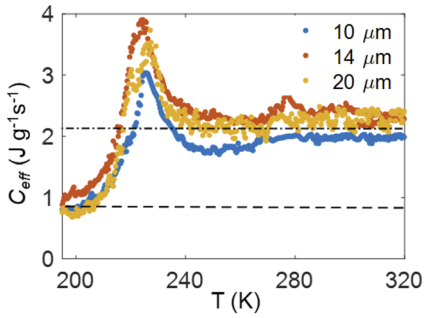

FIG. 6. The relaxation of C is also manifested in the thermal diffusion tail of the signal, via its influence on the effective thermal diffusivity, $\alpha_{eff} = \kappa/(\rho C_{eff})$. At the low and high temperature limits, the value of C_{eff} extracted from the thermal diffusion tail corresponds well to the respective asymptotic values C_0 and C_∞, indicated by the dashed–dotted and dashed line, respectively.

by DC volume dilatometry.[6] We pinpoint that dynamic dilatometry has also been introduced to perform thermal expansivity spectroscopy,[7,22,24] however, to the best of our knowledge, no dynamic or spectroscopic measurements has been reported on glycerol. The average values for C_0 and γ_0 from ISTS technique are 1980 ± 160 J kg^{-1} K^{-1} and $(5.5 \pm 0.7) \times 10^{-4}$ K^{-1}, respectively. The average ratios $\Delta C/C_\infty$ and $\Delta\gamma/\gamma_\infty$ are 1.2 ± 0.2 and 4.9 ± 0.7 for C and γ, respectively. As mentioned in Sec. III D, it is not possible to extract γ_∞ through fitting due to the degeneracy/mathematical compensation with the pre-factors in our model. We hence assigned to it a value of 10^{-4} K^{-1}, taken from the literature.[6]

One can further calculate the relaxation strength (R_S), defined as $\Delta C/C_0$ and $\Delta\gamma/\gamma_0$, 0.5 ± 0.1 and 0.81 ± 0.04. By fitting with SE model, the Debye–Waller factor,[14] $B/(A+B)$ in Eq. (40), is used to describe the relaxation strength, and we found a value of about 0.65 ± 0.05, which is in good agreement with the one (0.66 ± 0.05) reported in Ref. 14. The value lies in between the relaxation strength of C and γ. This result is somewhat expected since the two relaxing quantities are implicitly incorporated together into a single stretched exponential function. The relative relaxation strength of the thermal expansion is larger than the one of the specific heat capacity, implying that changing the volume by re-configuring the network is energetically more efficient than by increasing the occupancy of high energy anharmonic vibrations.

Interestingly, the asymptotic values of the specific heat can also be extracted, independently of the used models, from the temperature dependence of the thermal diffusion tail of the signal, as depicted in Fig. 6. Provided the relaxation time of the specific heat and thermal expansion occurs before or after the time window of the thermal diffusion tail, the signal tail is proportional to $\exp(-q^2\alpha_{eff}t)$, with α_{eff} an effective thermal diffusivity value connected to the specific heat via $\alpha_{eff} = \kappa_T/(\rho C_{eff})$, κ_T and ρ denote thermal conductivity and mass density, respectively. In light of their weak temperature dependence,[6,58] in this work, the latter two parameters have been assumed as constant, as 0.29 W m^{-1} K^{-1} and 1260 kg m^{-3}, respectively. Figure 6 reports C_{eff} as a function of temperature for the three gratings. The asymptotic values of C for low and high temperatures were found to be 960 ± 20 and 2190 ± 30 J kg^{-1} K^{-1}, as indicated by the two horizontal dashed lines, corresponding to a relaxation strength of 0.56, consistent with the value of 0.53 obtained from fitting with the model.

The SE model assumes that the relaxation for C and γ occur on the same time scale and connects their contribution to the ISTS signal via a single stretched exponential function. In order to experimentally verify whether the two response functions are indeed characterized by the same time scale and to what extent they can be disentangled, in Fig. 7, we compare the characteristic relaxation of the specific heat capacity and of the thermal expansion coefficient defined as $\omega_C/2\pi$ and $\omega_\gamma/2\pi$, respectively, both in the framework of Debye and HN models, with the relaxation frequency Γ_R of the SE model.

In the case of the Debye model [Fig. 7(a)], the specific heat capacity relaxation frequency (orange squares) is systematically higher, about a factor of 1.5 ± 0.1, than the one of the thermal expansion coefficient (blue diamonds). At first sight, one could conclude

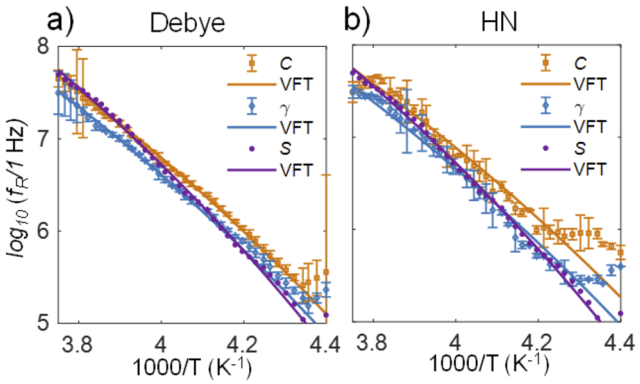

FIG. 7. Comparison of the temperature-dependent relaxation frequency f_R of specific heat C (orange) and thermal expansion coefficient γ (blue) extracted through the Debye model (a) and the HN model (b) and their fit with VFT (solid lines). The structural relaxation S (purple) extracted through the SE model is also given for comparison.

that after photothermally supplying energy, heat is first transferred from vibrational energy levels to configurational energy changes and, a somewhat later time, the configurational energy changes result in an increase in the volume. Similar conclusions can be drawn from the results obtained by the HN model, as shown in Fig. 7(b).

However, the results from HN model fitting are more dispersed due to the co-variance with the additional fitting variables, namely, exponents of a and b in the HN model, Eqs. (12) and (38). The obtained HN exponents turn out to be dispersed without showing any systematic temperature dependence. This could be expected since also no temperature dependence was found for stretched exponential ($\beta = 0.60 \pm 0.05$) in the SE model fitting in this work and also in Ref. 14. The obtained two HN coefficients (a and b) are 0.8 ± 0.2 and 0.7 ± 0.2 for the specific heat, and 0.8 ± 0.1 and 0.9 ± 0.1 for the thermal expansion. According to the relation between HN and KWW stretched exponential model,[42] $a \times b = \beta^{1.23}$, we estimate the corresponding stretched exponents $\beta_C = 0.63$ for specific heat and $\beta_\gamma = 0.77$. The two estimated values are slightly different with the value, $\beta = 0.60 \pm 0.05$, obtained from the single stretched exponential model fitting. The structural relaxation frequency obtained by fitting the experimental data with the SE model, via $\Gamma_R\beta/\Gamma(1/\beta)$,[14] with Γ denoting the gamma function, characterizes the (combined specific heat and thermal expansion coefficient) structural relaxation and turns out to lie somewhat in between the other two relaxation frequencies. The obtained temperature dependence of the relaxation frequencies was fitted to the Vogel–Fulcher–Tamman (VFT) equation (solid lines in Fig. 7), defined by $f_{relax} = f_0 \exp[-B/(T - T_0)]$, with f_0 being the relaxation frequency in the high temperature limit and T_0 being the Vogel–Fulcher temperature, around 130 K for glycerol. In Table IV, we report the fitted VFT parameters based on Debye, HN, and SE models. The results for the latter model are in line with the values reported in Ref. 14.

E. Comparison of thermal, mechanical, and dielectric relaxation

An apparent benefit of the disentangled physical model developed in this work is that it provides a way to assess the relaxation of specific heat and thermal expansion coefficient toward a frequency regime, 100 kHz to sub-100 MHz, that was previously inaccessible by any other means. This has allowed us to compare the slowing down of the structural relaxation upon cooling probed with thermal (all degrees of motion), mechanical (translational motion), and dielectric (rotational motion) susceptibilities. Indeed, the value of the structural relaxation time/frequency at a given temperature depends on the experimental observables and can differ by up to several decades.[7] This difference is referred to as time scale decoupling. There is so far no theory to interpret the decoupling among relaxation functions and to explain why some are faster than others. Several possible origins of the decoupling were discussed in Ref. 61. It should be emphasized that, in the absence of β-relaxation,[62] regardless of which relaxing quantity is investigated, the rate of the slowing down of the α-relaxation time, or the steepness and curvature of the VFT plots, upon cooling is expected to be identical.[5,63] For glycerol, this has been primarily validated among mechanical modulus measured by rheometry,[64] ultrasonic spectroscopy,[53] and Brillouin spectroscopy[5,61] and permittivity measured by dielectric spectroscopy.[65] Our results further enrich the validation with additional data from specific heat and thermal expansion spectroscopy up to sub-100 MHz. In view of the above, we have calculated the so-called fragility index m that characterizes the steepness of the VFT plot from the VFT fitting parameters shown in Table IV using the expression[65] $m = 16 + 590/D$ with $D = B/T_0$. The fragility values, obtained with our model, are summarized in Table IV and are close to 50, the latter being the fragility for glycerol reported in Refs. 65 and 66.

Interestingly, the model and results presented here allow us to test the so-called time scale ordering (TSO) regime in glycerol.[25] TSO regime occurs when the relaxation times for the shear modulus (G), bulk modulus (K), dielectric permittivity (ε), thermal expansivity coefficient (γ), and specific heat capacity (C) are ordered in the following way: $\tau_G < \tau_K < \tau_\varepsilon < \tau_\gamma < \tau_C$.[25] From an equivalent point of view, for a given temperature, the relaxation frequency follows the order $f_G > f_K > f_\varepsilon > f_\gamma > f_C$. TSO has been observed for three van der Waals bonded liquids (i.e., silicon oils DC704, 5PPE, and squalane) and for one hydrogen-bonded liquid (hexanetriol). So far, this has not yet been tested on glycerol.

TABLE IV. Comparison between fitted VFT parameters for heat capacity and thermal expansion obtained in this work using the Debye- and HN-based ISTS models (the first five rows) and VFT parameters for the heat capacity (determined by thermal effusivity photopyroelectric results reported in Bentefour *et al.*[20,21]), mechanical compliance (extracted from Jeong *et al.*[53]), and dielectric permittivity (extracted from Lunkenheimer *et al.*[60]).

Relaxation dynamics	Technique	$\log_{10}[f_0/(1\text{ Hz})]$	B (K)	T_{VFT} (K)	Fragility	Temperature range (K)
Heat capacity C (Debye)	ISTS	14.5	2140	127	51	230–260
Heat capacity C (HN)	ISTS	14.5	2100	124	51	230–260
Thermal expansion γ (Debye)	ISTS	13.9	2011	130	54	230–260
Thermal expansion γ (HN)	ISTS	13.9	2195	125	50	230–260
Structural ($C - \gamma$ mixed) (KWW)	ISTS	14.8	2138	135	53	230–260
Structural ($C - \gamma$ mixed)[14]	ISTS	14.7	2210	133	52	220–270
Heat capacity C[20,21]	PPE	11.9	1593	142	69	195–240
Heat capacity C[56,59]	3ω	14.6	2500	128	46	195–230
Mechanical compliance J[53]	US	14.4	2310	129	49	240–273
Dielectric permittivity ε[60]	DS	14.0	2309	129	49	200–285

Figure 8 summarizes VFT plots for properties of glycerol measured through dielectric spectroscopy (DS), ultrasonic spectroscopy (US), 3ω-specific heat spectroscopy, photopyroelectric (PPE) thermal spectroscopy, and ISTS (results of this work. For this analysis, we consider the Debye model). f_G was investigated in Ref. 5, but we could not add it to the current comparison because it was not fitted to the VFT equation. We also could not find available f_K to extract for the comparison. Nevertheless, f_J was shown as an alternative mechanical relaxation quantity.[53] J and K are a pair of reciprocal relaxing quantities and their relaxing frequencies are different, as explained later on.

At first glance, the available VFT plots (summarized in Fig. 8) turn out not to follow the TSO. This is perhaps not surprising, as there are several factors that can affect the determination of Arrhenius plots in practice. Those are related to experimental settings (e.g., uncertain temperature control and measurement and sample purity) and data processing (e.g., the relaxation frequency obtained via the KWW model can differ from the one obtained when assuming the HN model[42]). The discrepancy between the relaxation time values of C measured by different techniques is possibly caused not only by imperfect DC temperature control but also by the accumulated (electrical or laser) heating during experiments.

Moreover, it should be noted that when comparing two reciprocal relaxing quantities, a difference in relaxation time can also simply arise from purely mathematical reasons. Considering a relaxing observable $A(\omega)$ obeying the Debye relaxation model $A(\omega) = A_\infty + \frac{\Delta A}{1+i\omega/\omega_A}$, its inverse $B(\omega) = 1/A(\omega)$ can be rewritten as $1/A_\infty - \frac{\Delta A/A_0}{1+i\omega/(\omega_A A_0/A_\infty)}$. Clearly, the determined relaxation frequency of $B(\omega)$, $\omega_A A_0/A_\infty$, differs with the one of $A(\omega)$ by a factor identical to the ratio of the low-frequency limit response to the high-frequency limit response. This point also makes it, e.g., inadequate to compare in Fig. 8 the relaxation rate of mechanical compliance (J, green) with the one of the bulk modulus (used in TSO) and the others.

What comes as a surprise is that in our work the obtained f_C (red) is systematically faster than f_γ (blue), namely, $f_\gamma < f_C$. The values of these two relaxation frequencies were extracted from the same ISTS signal trace, excluding possible ambiguities concerning the sample and the temperature control over it. Moreover, the two quantities were extracted via the same relaxation model. This ISTS result is in contradiction with the trend suggested in Ref. 25, i.e., $f_\gamma > f_C$.

In order to further check our finding, we have evaluated the influence of the ordering of C and γ on the fitting of experimental ISTS signals. The results are shown in Figs. 9(a) and 9(b) for fits based on the Debye and HN-based ISTS models, respectively. In the top plot of Fig. 9(a), the black dots represent the experimental ISTS trace recorded at 245 K and a grating spacing of 14 μm. The green line is the best fit. It results in a faster relaxation frequency for

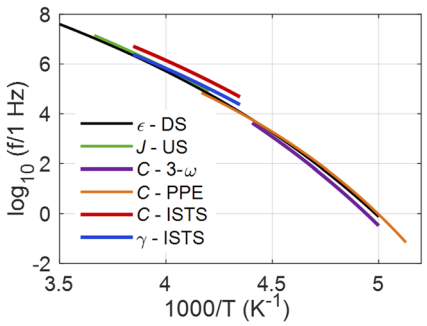

FIG. 8. Compilation of available VFT plots of glycerol measured by different relaxation quantities and techniques. VFT parameters of each are listed in Table IV.

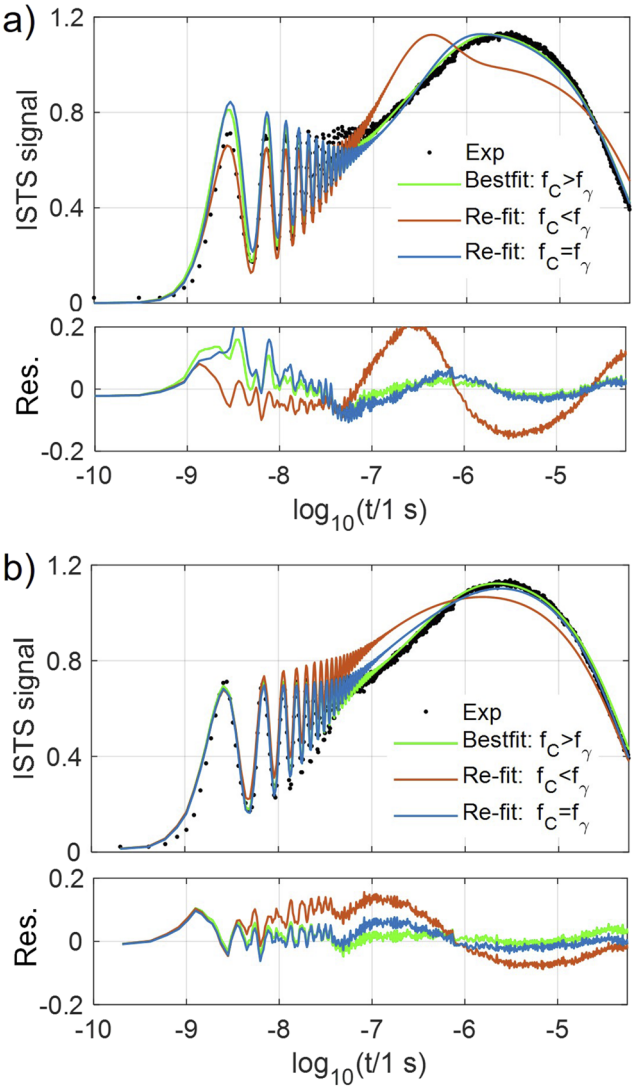

FIG. 9. Validation of the order of f_C and f_γ obtained by model fitting based on the Debye (a) and HN (b) models developed in this work. The black dots in the top plots of each panel are the experimental ISTS trace recorded at 245 K and grating spacing of 14 μm. The results show that better quality of fitting is achieved when $f_C > f_\gamma$ (green curves), compared to the case where $f_C < f_\gamma$ (orange curves) or $f_C = f_\gamma$ (blue curves). The fitting residuals (bottom plots in each panel) are calculated for each to indicate the fitting quality. The involved fitting parameters for each plot are given in Table V.

TABLE V. Fitting parameters corresponding to the plots in Fig. 9(a) based on the Debye–ISTS model and Fig. 9(b) based on the HN–ISTS model. In the HN model fitting, the obtained HN exponents [a, b] for the three cases are [0.85, 0.99], [0.93, 0.51], and [0.99, 0.50], respectively, for C and [0.85, 0.90], [0.56, 0.99], and [0.75, 0.99], respectively, for γ.

Debye–ISTS	$\log_{10}(f_C$ Hz)	$\log_{10}(f_\gamma$ Hz)	$\Delta C/C_\infty$	C_∞ (J/kg K)	$\Delta\gamma/\gamma_\infty$
Bestfit $f_C > f_\gamma$	6.52	6.32	2.1	820	6.6
Re-fit $f_C < f_\gamma$	6.32	6.52	1.6	1410	6.2
Re-fit $f_C = f_\gamma$	5.94	5.94	2.6	680	7.2
HN–ISTS	$\log_{10}(f_C$ Hz)	$\log_{10}(f_\gamma$ Hz)	$\Delta C/C_\infty$	C_∞ (J/kg K)	$\Delta\gamma/\gamma_\infty$
Bestfit $f_C > f_\gamma$	6.8	6.4	2.8	630	12.3
Re-fit $f_C < f_\gamma$	6.4	6.8	1.8	826	8.8
Re-fit $f_C = f_\gamma$	6.6	6.6	1.9	755	8.6

C, $\log_{10}(f_C) = 6.52 \pm 0.04$, than for γ, $\log_{10}(f_\gamma) = 6.33 \pm 0.02$. When applying a forced switch between the values of the two relaxation frequencies, it turns out that it is not possible to re-fit with equal quality the signal (orange line), also when leaving the other parameters free. In addition, when forcing the two relaxation frequencies to be equal and performing a full fit, there is an obvious decline in fitting quality (blue line). The residuals of each fitting attempt are plotted in the bottom panel. The corresponding parameters are listed in Table V. When assuming a HN–ISTS model, due to the higher number of fitting parameters, the fitting quality improves [Fig. 9(b)]. In addition, in that case, the comparison of the fitting quality between the different assumptions shows a best fit for $f_C > f_\gamma$, with $\log_{10}(f_C) = 6.8 \pm 0.2$ and $\log_{10}(f_\gamma) = 6.4 \pm 0.1$.

VI. CONCLUSION

A model to describe ISTS signals generated in relaxing materials has been introduced. The model is based on the solution of the thermal diffusion and continuum mechanics equations, upon insertion of frequency-dependent specific heat and thermal expansion coefficients. The latter two were cast in the form of Debye and Havriliak–Negami expressions, respectively. The proposed models were first shown to effectively fit ISTS signals for glycerol that had been generated, for different temperature–wavenumber combinations, by a model[18] that has been historically used to describe ISTS signals in relaxing materials and that makes use of a stretched exponential function. Furthermore, we performed ISTS experiments on glycerol under supercooling conditions. We fitted the data with the models here developed. We compared the results against the one obtained exploiting the often-used SE model. Satisfactory fitting quality was achieved for all ISTS waveforms, supporting the validity of the models developed in this work. Furthermore, we were able to investigate the relaxation of C and γ, up to several tens of MHz, greatly extending the upper frequency bound so far achieved by thermal susceptibility spectroscopy, by nearly 3 and 7 decades for $C(\omega)$ and $\gamma(\omega)$, respectively. The best fit results suggest that the relaxation strength of thermal expansion, 0.8, is significantly larger than the one of the specific heat, 0.5, implying that changing the volume by re-configuring the network is more efficient than by increasing the occupancy of high energy anharmonic vibrations. The findings of this work are in line with an accompanying work,[55] in which a transient thermal lens technique is used to time resolve the relaxation of specific heat and thermal expansion. We have also compared the obtained VFT plots of the specific heat and the thermal expansion with those of the mechanical compliance and dielectric permittivity reported in the literature. A similar steepness or curvature has been found for those different VFT plots, which confirms once more that the fragility (curvature of the Arrhenius plot) for a given material is universal between the different response functions, in spite of the characteristic relaxation frequencies being somewhat different between physical susceptibilities. Due to ambiguous factors in the comparison of data extracted in different experimental circumstances, our results do not allow for a fully conclusive test for glycerol on a recently identified phenomenological trend of time scale ordering (TSO) in other glass formers.[25] However, the ISTS measurements as well as the measurements reported in Ref. 55 do suggest for glycerol that the relaxation of C occurs slightly faster than γ, which is in apparent contradiction with the tendency reported in Ref. 25. Nevertheless, given the complexity (multiparametric fitting) in disentangling the relaxation of C and γ in ISTS response and possible effects of inaccuracies in the modeling of the frequency dependence of the signal detection system, further systematic and rigorous validations of the TSO paradigms on glycerol would be desirable, with special care concerning the quality of temperature control, the sample purity, and the influence of the choice of relaxation models and the type experimental implementation (frequency domain or time domain).

SUPPLEMENTARY MATERIAL

See the supplementary material for (I) technical details of implementing the residue theorem, (II) the existing SE model and a possible pitfall, and (III) evaluation of fitting uncertainty with least-squares and most-squares error analysis, and (IV) movies of a full presentation of the best fit results by three models, illustrated in Fig. 3.

ACKNOWLEDGMENTS

C.G. and M.G. acknowledge financial support from the KU Leuven Research Council (Grant No. C14/16/063)

(OPTIPROBE). M.G. acknowledges financial support from the CNR Joint Laboratories program 2019–2021, Project No. SAC.AD002.026 (OMEN). L.L. acknowledges financial support from the FWO (Research Foundation-Flanders) postdoctoral research fellowship (Grant Nos. 12V4419N and 12V4422N). P.Z. acknowledges the support of the Chinese Scholarship Council (CSC). F.B. acknowledges financial support from the Université de Lyon in the frame of the IDEXLYON Project (Grant No. ANR-16-IDEX-0005) and from Université Claude Bernard Lyon 1 through the BQR Accueil EC 2019 grant.

AUTHOR DECLARATIONS

Conflict of Interest

The authors have no conflicts to disclose.

DATA AVAILABILITY

The data that support the findings of this study are available from the corresponding authors upon reasonable request.

REFERENCES

[1]C. Scalliet, B. Guiselin, and L. Berthier, "Excess wings and asymmetric relaxation spectra in a facilitated trap model," arXiv:2106.01759 (2021).
[2]V. Bapst, T. Keck, A. Grabska-Barwińska, C. Donner, E. D. Cubuk, S. S. Schoenholz, A. Obika, A. W. R. Nelson, T. Back, D. Hassabis *et al.*, "Unveiling the predictive power of static structure in glassy systems," Nat. Phys. **16**, 448–454 (2020).
[3]M. H. Jensen, C. Gainaru, C. Alba-Simionesco, T. Hecksher, and K. Niss, "Slow rheological mode in glycerol and glycerol–water mixtures," Phys. Chem. Chem. Phys. **20**, 1716–1723 (2018).
[4]T. Hecksher, D. H. Torchinsky, C. Klieber, J. A. Johnson, J. C. Dyre, and K. A. Nelson, "Toward broadband mechanical spectroscopy," Proc. Natl. Acad. Sci. U. S. A. **114**, 8710–8715 (2017).
[5]C. Klieber, T. Hecksher, T. Pezeril, D. H. Torchinsky, J. C. Dyre, and K. A. Nelson, "Mechanical spectra of glass-forming liquids. II. Gigahertz-frequency longitudinal and shear acoustic dynamics in glycerol and DC704 studied by time-domain Brillouin scattering," J. Chem. Phys. **138**, 12A544 (2013).
[6]I. V. Blazhnov, N. P. Malomuzh, and S. V. Lishchuk, "Temperature dependence of density, thermal expansion coefficient and shear viscosity of supercooled glycerol as a reflection of its structure," J. Chem. Phys. **121**, 6435–6441 (2004).
[7]K. Niss and T. Hecksher, "Perspective: Searching for simplicity rather than universality in glass-forming liquids," J. Chem. Phys. **149**, 230901 (2018).
[8]C. Klieber, V. E. Gusev, T. Pezeril, and K. A. Nelson, "Nonlinear acoustics at GHz frequencies in a viscoelastic fragile glass former," Phys. Rev. Lett. **114**, 065701 (2015).
[9]D. Gundermann, U. R. Pedersen, T. Hecksher, N. P. Bailey, B. Jakobsen, T. Christensen, N. B. Olsen, T. B. Schrøder, D. Fragiadakis, R. Casalini *et al.*, "Predicting the density-scaling exponent of a glass-forming liquid from Prigogine–Defay ratio measurements," Nat. Phys. **7**, 816–821 (2011).
[10]C. Glorieux, K. A. Nelson, G. Hinze, and M. D. Fayer, "Thermal, structural, and orientational relaxation of supercooled salol studied by polarization-dependent impulsive stimulated scattering," J. Chem. Phys. **116**, 3384–3395 (2002).
[11]S. M. Silence, A. R. Duggal, L. Dhar, and K. A. Nelson, "Structural and orientational relaxation in supercooled liquid triphenylphosphite," J. Chem. Phys. **96**, 5448–5459 (1992).
[12]Y. Yang and K. A. Nelson, "T_c of the mode coupling theory evaluated from impulsive stimulated light scattering on salol," Phys. Rev. Lett. **74**, 4883 (1995).
[13]Y. Yang and K. A. Nelson, "Impulsive stimulated light scattered from glass-forming liquids. II. Salol relaxation dynamics, nonergodicity parameter, and testing of mode coupling theory," J. Chem. Phys. **103**, 7732–7739 (1995).
[14]D. M. Paolucci and K. A. Nelson, "Impulsive stimulated thermal scattering study of structural relaxation in supercooled glycerol," J. Chem. Phys. **112**, 6725–6732 (2000).
[15]I. C. Halalay and K. A. Nelson, "The liquid–glass transition in $LiCl/H_2O$: Impulsive stimulated light scattering experiments and mode-coupling analysis," J. Chem. Phys. **97**, 3557–3572 (1992).
[16]I. C. Halalay and K. A. Nelson, "Time-resolved spectroscopy and scaling behavior in $LiCl/H_2O$ near the liquid–glass transition," Phys. Rev. Lett. **69**, 636 (1992).
[17]S. M. Silence, S. R. Goates, and K. A. Nelson, "Impulsive stimulated scattering study of normal and supercooled liquid triphenylphosphite," Chem. Phys. **149**, 233–259 (1990).
[18]Y. Yang and K. A. Nelson, "Impulsive stimulated light scattering from glass-forming liquids. I. Generalized hydrodynamics approach," J. Chem. Phys. **103**, 7722–7731 (1995).
[19]N. O. Birge and S. R. Nagel, "Specific-heat spectroscopy of the glass transition," Phys. Rev. Lett. **54**, 2674 (1985).
[20]E. H. Bentefour, C. Glorieux, M. Chirtoc, and J. Thoen, "Broadband photopyroelectric thermal spectroscopy of a supercooled liquid near the glass transition," J. Appl. Phys. **93**, 9610–9614 (2003).
[21]E. H. Bentefour, C. Glorieux, M. Chirtoc, and J. Thoen, "Thermal relaxation of glycerol and propylene glycol studied by photothermal spectroscopy," J. Chem. Phys. **120**, 3726–3731 (2004).
[22]K. Niss, D. Gundermann, T. Christensen, and J. C. Dyre, "Dynamic thermal expansivity of liquids near the glass transition," Phys. Rev. E **85**, 041501 (2012).
[23]L. Liu, M. Gandolfi, R. Salenbien, F. Banfi, and C. Glorieux, "Scrutinizing laser induced thermal expansion in a supercooled glassy system: Entangled relaxation of specific heat capacity and thermal expansivity" (unpublished).
[24]C. Bauer, R. Böhmer, S. Moreno-Flores, R. Richert, H. Sillescu, and D. Neher, "Capacitive scanning dilatometry and frequency-dependent thermal expansion of polymer films," Phys. Rev. E **61**, 1755 (2000).
[25]L. A. Roed, J. C. Dyre, K. Niss, T. Hecksher, and B. Riechers, "Time-scale ordering in hydrogen- and van der Waals-bonded liquids," J. Chem. Phys. **154**, 184508 (2021).
[26]M. Gandolfi, G. Benetti, C. Glorieux, C. Giannetti, and F. Banfi, "Accessing temperature waves: A dispersion relation perspective," Int. J. Heat Mass Transfer **143**, 118553 (2019).
[27]M. Gandolfi, C. Giannetti, and F. Banfi, "Temperonic crystal: A superlattice for temperature waves in graphene," Phys. Rev. Lett. **125**, 265901 (2020).
[28]M. Celebrano, D. Rocco, M. Gandolfi, A. Zilli, F. Rusconi, A. Tognazzi, A. Mazzanti, L. Ghirardini, E. A. A. Pogna, L. Carletti *et al.*, "Optical tuning of dielectric nanoantennas for thermo-optically reconfigurable nonlinear metasurfaces," Opt. Lett. **46**, 2453–2456 (2021).
[29]M. Gandolfi, A. Tognazzi, D. Rocco, C. De Angelis, and L. Carletti, "Near-unity third-harmonic circular dichroism driven by a quasibound state in the continuum in asymmetric silicon metasurfaces," Phys. Rev. A **104**, 023524 (2021).
[30]A. Ronchi, A. Sterzi, M. Gandolfi, A. Belarouci, C. Giannetti, N. Del Fatti, F. Banfi, and G. Ferrini, "Discrimination of nano-objects via cluster analysis techniques applied to time-resolved thermo-acoustic microscopy," Ultrasonics **114**, 106403 (2021).
[31]A. Tognazzi, D. Rocco, M. Gandolfi, A. Locatelli, L. Carletti, and C. De Angelis, "High quality factor silicon membrane metasurface for intensity-based refractive index sensing," Optics **2**, 193–199 (2021).
[32]J. Fivez, R. Salenbien, M. K. Malayil, W. Schols, and C. Glorieux, "Dynamics of specific heat and other relaxation processes in supercooled liquids by impulsive stimulated scattering," J. Phys.: Conf. Ser. **278**, 012021 (2011).
[33]S. Havriliak and S. Negami, "A complex plane analysis of α-dispersions in some polymer systems," J. Polym. Sci., Part C: Polym. Symp. **14**, 99–117 (1966).
[34]B. A. Auld, *Acoustic Fields and Waves in Solids* (John Wiley & Sons, 1973).
[35]M. Gandolfi, F. Banfi, and C. Glorieux, "Optical wavelength dependence of photoacoustic signal of gold nanofluid," Photoacoustics **20**, 100199 (2020).
[36]S. Mukhopadhyay, "Relaxation effects on thermally induced vibrations in a generalized thermoviscoelastic medium with a spherical cavity," J. Therm. Stresses **22**, 829–840 (1999).

[37]M. I. A. Othman and I. A. Abbas, "Fundamental solution of generalized thermo-viscoelasticity using the finite element method," Comput. Math. Model. **23**, 158–167 (2012).
[38]As indicated on p. 88 of Ref. 34, the viscosity tensor has the same form of the stiffness matrix. Hence, we can write the viscosity tensor as $\eta = \tau_\eta C$, where C is the stiffness matrix.[36,37]
[39]Y. X. Yan and K. A. Nelson, "Impulsive stimulated light scattering. I. General theory," J. Chem. Phys. **87**, 6240–6256 (1987).
[40]M. Gupta and N. Kumar, "Scope and opportunities of using glycerol as an energy source," Renewable Sustainable Energy Rev. **16**, 4551–4556 (2012).
[41]Since in this work we study the ISTS signal detected with a heterodyne experimental setup, the right-hand-side of Eq. (40) is not squared. This choice is at variance with respect to Ref. 14, which is based on homodyne detection.
[42]F. Alvarez, A. Alegra, and J. Colmenero, "Relationship between the time-domain Kohlrausch–Williams–Watts and frequency-domain Havriliak–Negami relaxation functions," Phys. Rev. B **44**, 7306 (1991).
[43]D. D. Jackson, "Most squares inversion," J. Geophys. Res. **81**, 1027–1030, https://doi.org/10.1029/jb081i005p01027 (1976).
[44]R. Salenbien, R. Côte, J. Goossens, P. Limaye, R. Labie, and C. Glorieux, "Laser-based surface acoustic wave dispersion spectroscopy for extraction of thicknesses, depth, and elastic parameters of a subsurface layer: Feasibility study on intermetallic layer structure in integrated circuit solder joint," J. Appl. Phys. **109**, 093104 (2011).
[45]H. Ren, S. Xu, Y. Liu, and S.-T. Wu, "Liquid-based infrared optical switch," Appl. Phys. Lett. **101**, 041104 (2012).
[46]B. Verstraeten, J. Sermeus, R. Salenbien, J. Fivez, G. Shkerdin, and C. Glorieux, "Determination of thermoelastic material properties by differential heterodyne detection of impulsive stimulated thermal scattering," Photoacoustics **3**, 64–77 (2015).
[47]A. Vega-Flick, J. K. Eliason, A. A. Maznev, A. Khanolkar, M. Abi Ghanem, N. Boechler, J. J. Alvarado-Gil, and K. A. Nelson, "Laser-induced transient grating setup with continuously tunable period," Rev. Sci. Instrum. **86**, 123101 (2015).
[48]A. A. Maznev, K. A. Nelson, and J. A. Rogers, "Optical heterodyne detection of laser-induced gratings," Opt. Lett. **23**, 1319–1321 (1998).
[49]P. Brodard and E. Vauthey, "Application of transient evanescent grating techniques to the study of liquid/liquid interfaces," J. Phys. Chem. B **109**, 4668–4678 (2005).
[50]A. Taschin, R. Eramo, P. Bartolini, and R. Torre, *Time-Resolved Spectroscopy in Complex Liquids* (Springer, 2008); available at https://link.springer.com/book/10.1007%2F978-0-387-25558-3.
[51]A. J. Liu and S. R. Nagel, "Jamming is not just cool any more," Nature **396**, 21–22 (1998).
[52]L. Liu, K. Zhong, T. Munro, S. Alvarado, R. Côte, S. Creten, E. Fron, H. Ban, M. Van der Auweraer, N. B. Roozen *et al.*, "Wideband fluorescence-based thermometry by neural network recognition: Photothermal application with 10 ns time resolution," J. Appl. Phys. **118**, 184906 (2015).
[53]Y. H. Jeong, S. R. Nagel, and S. Bhattacharya, "Ultrasonic investigation of the glass transition in glycerol," Phys. Rev. A **34**, 602 (1986).
[54]B. Schroyen, D. Vlassopoulos, P. Van Puyvelde, and J. Vermant, "Bulk rheometry at high frequencies: A review of experimental approaches," Rheol. Acta **59**, 1–22 (2020).
[55]P. Zhang, M. Gandolfi, F. Banfi, C. Glorieux, and L. Liu, "Time-resolved thermal lens investigation of glassy dynamics in supercooled liquids: Theory and experiments," J. Chem. Phys. **155**, 074503 (2021).
[56]N. O. Birge, "Specific-heat spectroscopy of glycerol and propylene glycol near the glass transition," Phys. Rev. B **34**, 1631 (1986).
[57]L.-M. Wang, V. Velikov, and C. A. Angell, "Direct determination of kinetic fragility indices of glassforming liquids by differential scanning calorimetry: Kinetic versus thermodynamic fragilities," J. Chem. Phys. **117**, 10184–10192 (2002).
[58]A. A. Minakov, S. A. Adamovsky, and C. Schick, "Simultaneous measurements of complex heat capacity and complex thermal conductivity by two-channel AC calorimeter," Thermochim. Acta **377**, 173–182 (2001).
[59]N. O. Birge, P. K. Dixon, and N. Menon, "Specific heat spectroscopy: Origins, status and applications of the 3ω method," Thermochim. Acta **304–305**, 51–66 (1997).
[60]P. Lunkenheimer, U. Schneider, R. Brand, and A. Loid, "Glassy dynamics," Contemp. Phys. **41**, 15–36 (2000).
[61]L. Comez, D. Fioretto, F. Scarponi, and G. Monaco, "Density fluctuations in the intermediate glass-former glycerol: A Brillouin light scattering study," J. Chem. Phys. **119**, 6032–6043 (2003).
[62]R. Richert and C. A. Angell, "Dynamics of glass-forming liquids. V. On the link between molecular dynamics and configurational entropy," J. Chem. Phys. **108**, 9016–9026 (1998).
[63]B. Jakobsen, T. Hecksher, T. Christensen, N. B. Olsen, J. C. Dyre, and K. Niss, "Communication: Identical temperature dependence of the time scales of several linear-response functions of two glass-forming liquids," J. Chem. Phys. **136**, 081102 (2012).
[64]X. Shi, A. Mandanici, and G. B. McKenna, "Shear stress relaxation and physical aging study on simple glass-forming materials," J. Chem. Phys. **123**, 174507 (2005).
[65]R. Böhmer, K. L. Ngai, C. A. Angell, and D. J. Plazek, "Nonexponential relaxations in strong and fragile glass formers," J. Chem. Phys. **99**, 4201–4209 (1993).
[66]S. A. Hutcheson and G. B. McKenna, "The measurement of mechanical properties of glycerol, *m*-toluidine, and sucrose benzoate under consideration of corrected rheometer compliance: An in-depth study and review," J. Chem. Phys. **129**, 074502 (2008).